



Analysis of gas transport behavior in organic and inorganic nanopores based on a unified apparent gas permeability model

Qi Zhang¹ · Wen-Dong Wang² · Yilihamu Kade³ · Bo-Tao Wang⁴ · Lei Xiong⁵

Received: 20 January 2019
© The Author(s) 2019

Abstract

Different from the conventional gas reservoirs, gas transport in nanoporous shales is complicated due to multiple transport mechanisms and reservoir characteristics. In this work, we presented a unified apparent gas permeability model for real gas transport in organic and inorganic nanopores, considering real gas effect, organic matter (OM) porosity, Knudsen diffusion, surface diffusion, and stress dependence. Meanwhile, the effects of monolayer and multilayer adsorption on gas transport are included. Then, we validated the model by experimental results. The influences of pore radius, pore pressure, OM porosity, temperature, and stress dependence on gas transport behavior and their contributions to the total apparent gas permeability (AGP) were analyzed. The results show that the adsorption effect causes $Kn(OM) > Kn(IM)$ when the pore pressure is larger than 1 MPa and the pore radius is less than 100 nm. The ratio of the AGP over the intrinsic permeability decreases with an increase in pore radius or pore pressure. For nanopores with a radius of less than 10 nm, the effects of the OM porosity, surface diffusion coefficient, and temperature on gas transport cannot be negligible. Moreover, the surface diffusion almost dominates in nanopores with a radius less than 2 nm under high OM porosity conditions. For the small-radius and low-pressure conditions, gas transport is governed by the Knudsen diffusion in nanopores. This study focuses on revealing gas transport behavior in nanoporous shales.

Keywords Gas transport · Apparent gas permeability model · Gas adsorption · Surface diffusion · Stress dependence

Qi Zhang and Wen-Dong Wang contributed equally to this work.

Edited by Yan-Hua Sun

✉ Qi Zhang
zhangqi6242006@gmail.com

- ¹ Key Laboratory of Tectonics and Petroleum Resources, China University of Geosciences, Wuhan 430074, Hubei, China
- ² School of Petroleum Engineering, China University of Petroleum (East China), Qingdao 266580, Shandong, China
- ³ Institute of Ground Engineering, Engineering Technology Research Institute of PetroChina Xinjiang Oilfield Company, Karamay 834000, Xinjiang, China
- ⁴ Oil Production Plant 5 of PetroChina Changqing Oilfield Company, Changqing Oilfield, Xi'an 710200, Shaanxi, China
- ⁵ Oil Production Plant 1 of PetroChina Xinjiang Oilfield Company, Karamay 834000, Xinjiang, China

1 Introduction

In North America and China, shale gas with rich reserves and great potential has been developed efficiently (Su et al. 2015). The multiple gas transport mechanisms and reservoir features of the shales are different from those of other unconventional reservoirs. Therefore, it is essential to figure out the complicated gas transport behavior in nanoporous shales on the basis of physical experiments (Wang et al. 2015, 2016a, 2017), numerical methods (Botan et al. 2013; Chen et al. 2015; Sun et al. 2017; Wu et al. 2015a, b, c; Yao et al. 2013), and theoretical apparent gas permeability (AGP) models. Experimental results (Ambrose et al. 2012; Zou et al. 2012) have shown that the pores in shale reservoirs range in nanoscale size (generally smaller than 5 nm), which causes the approximation between the molecular mean free path and shale nanopores size, and continuity assumption invalid (Song et al. 2016). Organic matter (OM) and inorganic matter (IM) have been observed in the typical shale samples, and the schematic diagram can be shown in Fig. 1.

The Knudsen number (Kn) is widely used to characterize the gas transport behavior in the microscale pores (Civan 2010; Civan et al. 2011, 2013). Different flow regimes can

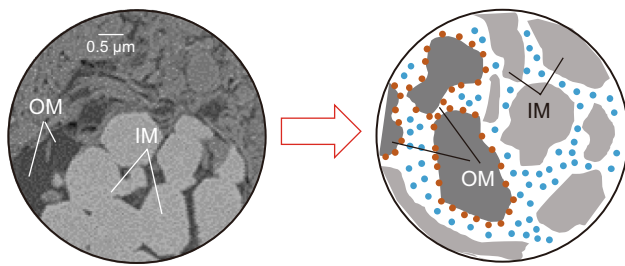


Fig. 1 2D FIB/SEM image and schematic diagram of a shale sample showing nanopores in OM and IM

be divided based on the Knudsen number Kn (the ratio of a molecular mean free path to the average pore diameter) (Wu et al. 2015c), including continuum flow ($Kn < 0.001$), slip flow ($0.001 < Kn < 0.1$), transition flow ($0.1 < Kn < 10$), and molecular scale flow ($Kn > 10$). Under typical shale gas reservoir conditions, Kn ranges from 0.0001 to 10 (Wu et al. 2014), which means continuum flow, slip flow, and transition flow coexist in shale nanopores. Moreover, Li et al. (2013) reported that the maximal proportion of adsorbed gas can reach around eighty percent of the total gas-in-place in shale gas reservoirs (Li et al. 2013). Adsorbed gas decreases the organic nanopore size, and the surface diffusion of adsorbed gas molecules will occur (Akkutulu and Fathi 2012). Therefore, scholars have proposed various AGP models to characterize gas transport mechanisms. Civan et al. developed the Beskok and Karniadakis (B–K) model (Beskok and Karniadakis 1999) into the characterization of gas transport in the porous media and presented the AGP models based on the Knudsen number, considering the viscous flow and the rarefaction effect. Xiong et al. (2012) and Sigal (2013) improved Civan’s models by taking the adsorbed gas into account. Based on the pore structure and Maxwell theory, Javadpour (2009) presented the AGP model with several empirical factors. Singh and Javadpour (2016) developed the AGP model by linear superposition of viscous

flow and Knudsen diffusion. In addition, although Wang et al. (2016b) derived the AGP model for real gas transport in nanopores, the Knudsen diffusion is ignored. Song et al. (2016) introduced the phase behavior and presented the AGP models for IM and OM, which ignored the structural parameters in the surface diffusion equation. Weighting coefficients relevant to Kn of different mechanisms are introduced into the AGP models by Shi et al. (2013) and Wu et al. (2015a, b, c, 2016, 2017). Few work (Shi et al. 2013; Zhang et al. 2017) focused on the effects of the OM porosity on the AGP of shale reservoirs. The comparison of different AGP models is shown in Table 1. In brief, an accurate AGP model is essential for the analysis of gas transport behavior in shale reservoirs.

Different from the previous work (Zhang et al. 2018), we modified a unified AGP model and focused on the comparison of different characterizations for the gas transport mechanisms, and more influences of various parameters on gas transport behavior are analyzed in this work. Viscous–slip flow, Knudsen diffusion, monolayer and multilayer gas adsorption, surface diffusion, the weighting coefficients of viscous–slip flow and Knudsen diffusion, and stress dependence are included in nanopores. The presented AGP model is validated by the experimental results. Then, on the one hand, the influences of Knudsen number, pore pressure, pore temperature, pore radius, OM porosity, and stress dependence on AGP are analyzed. On the other hand, the contributions of different mechanisms to the total AGP are conducted to reveal gas transport behavior. The proposed AGP model in this work is expected for macro-simulation for the development of shale reservoirs.

2 AGP mathematical model

The schematic diagram of gas transport in IM and OM nanopores is shown in Sects. 2.1 and 2.2. Some assumptions are as follows: single phase and isothermal methane transport

Table 1 Comparison of different AGP models

Model	Viscous–slip flow	Knudsen diffusion	Adsorption effect	Surface diffusion	Real gas effect	Stress dependence	OM porosity	Limitations
Beskok and Devegowda	✓	–	×	×	×	×	–	Empirical factors
Civan et al.	✓	–	×	×	×	×	–	Based on B–K model
Xiong et al.	✓	–	✓	×	×	×	–	Based on B–K model
Javadpour	✓	✓	×	×	×	×	–	Empirical factors
Darabi et al.	✓	✓	×	×	×	×	×	Based on Javadpour model
Singh and Javadpour	✓	–	–	✓	×	×	×	Linear superposition of multiple mechanisms
Shi et al.	✓	✓	×	×	×	×	✓	Gas–water phase
Wu et al.	✓	✓	✓	✓	✓	✓	×	–
Song et al.	✓	–	✓	✓	✓	✓	×	Based on B–K model
Wang et al.	✓	–	✓	✓	✓	×	×	Based on B–K model

in nanopores; there is no mass transfer between organic and inorganic pores; gas adsorption on pore wall surface follows BET isotherm equation in OM; porosity and tortuosity, surface diffusion, and OM porosity are considered. Then, we derived the AGP models.

2.1 Characterization of gas transport in IM

The real gas effect, viscous–slip flow, and Knudsen diffusion are considered in IM nanopores as shown in Fig. 2. The Knudsen number $Kn(IM)$ for gas transport in IM can be expressed as (Bird 1994; Michel et al. 2011)

$$Kn(IM) = \frac{\kappa_B TZ}{2\sqrt{2}\pi\delta^2 p r_{el}}, \tag{1}$$

where r_{el} is the effective inorganic pore radius, m; κ_B is the Boltzmann constant, MPa m³/K; T is the pore temperature, K; Z is the gas deviation factor, dimensionless; p is the pore pressure, MPa; and δ is molecular collision diameter, m.

For real gas, Z is related to $p_{pr} = \frac{p}{p_c}$ and $T_{pr} = \frac{T}{T_c}$ can be expressed as (Mahmoud 2014)

$$Z = 0.702p_{pr}^2 e^{-2.5T_{pr}} - 5.524p_{pr} e^{-2.5T_{pr}} + 0.044T_{pr}^2 - 0.164T_{pr} + 1.15 \tag{2}$$

where p_{pr} is the pseudo-reduced pressure, dimensionless; p_c is the critical pressure, MPa; T_{pr} is the pseudo-reduced temperature, K; and T_c is the critical temperature, K.

Lee et al. (1966) gave the expression of gas viscosity as

$$\mu = 10^{-13} \frac{(9.379 + 0.01607M)T^{1.5}}{209.2 + 19.26M + T} \exp \left[\left(3.448 + \frac{986.4}{T} + 0.01009M \right) \left(10^9 \frac{pM}{RZT} \right)^{(2.447-0.224X)} \right], \tag{3}$$

where μ is the gas viscosity, MPa s; ρ is gas density, kg/m³; M is the gas molar mass, kg/mol; and R is the gas universal constant, J/(mol K).

Because of the collision between gas molecules, the viscous–slip flow for gas transport in IM nanopores can be written as (Karniadakis et al. 2005; Wu et al. 2016)

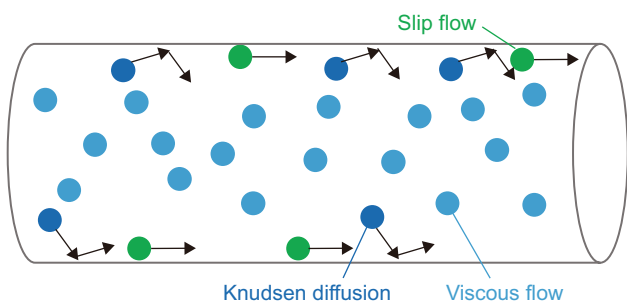


Fig. 2 Schematic diagram of gas transport in the IM nanopore

$$J_{v+s}^I = -\frac{\phi_e^I}{\tau} \frac{r_{el}^2 p M}{8\mu_e ZRT} \left(1 + \frac{4Kn(IM)}{1 - bKn(IM)} \right) \nabla p \tag{4}$$

where J_{v+s}^I is the viscous and slip flow mass flux in IM nanopores, kg/(m² s); ϕ_e^I is the effective porosity of IM, dimensionless; τ is the tortuosity, dimensionless; μ_e is the effective gas viscosity, MPa s; b is the slip coefficient, dimensionless (here, $b = -1$); and ∇p is the gas pressure gradient, MPa/m.

Considering the rarefied gas effect, if $\alpha = \frac{128}{15\pi^2} \tan^{-1}(4.0Kn^{0.4})$, Eq. (4) becomes (Beskok and Karniadakis 1999)

$$J_{v+s}^I = -\frac{\phi_e^I}{\tau} \frac{r_{el}^2 p M}{8\mu_e ZRT} (1 + \alpha Kn(IM)) \left(1 + \frac{4Kn(IM)}{1 - bKn(IM)} \right) \nabla p \tag{5}$$

Considering the collision between gas molecules and pore walls, Knudsen diffusion for real gas is given by (Darabi et al. 2012)

$$J_K^I = -\frac{\phi_e^I}{\tau} \frac{2r_{el}}{3} \left(\frac{8ZM}{\pi RT} \right)^{0.5} \frac{p}{Z} C_g \nabla p \tag{6}$$

where J_K^I is the Knudsen diffusion mass flux in IM, kg/(m² s); $C_g = \left(\frac{1}{p} - \frac{1}{Z} \frac{dZ}{dp} \right)$; D_m is the methane molecule diameter, m; for characterizing various transport mechanism weight on gas transport, weighting coefficients of viscous–slip flow, and Knudsen diffusion were presented (Shi et al. 2013; Wu et al. 2016). Thus, the total mass flux of free gas in IM pores can be expressed as

$$J^I = \omega_{v+s} J_{v+s}^I + \omega_K J_K^I \tag{7}$$

where J^I is the mass flux in IM nanopores kg/(m² s).

Two terms of the weighting coefficients based on the Knudsen number Kn reported (Shi et al. 2013; Wu et al. 2016) are listed as follows:

$$\omega_{v+s} = \frac{1}{1 + (Kn/Kn_{0.5})^{\bar{n}-1}}, \quad \omega_K = \frac{1}{1 + (Kn/Kn_{0.5})^{1-\bar{n}}}, \tag{8}$$

$$\omega_{v+s} = \frac{1}{1 + Kn}, \quad \omega_K = \frac{1}{1 + 1/Kn}, \tag{9}$$

where ω_{v+s} is the weighting coefficient of viscous and slip flow, dimensionless; ω_K is the weighting coefficient of the Knudsen number, dimensionless; and $\bar{n} = 5$, $Kn_{0.5} = 4.5$ (Shi et al. 2013).

Figure 3 illustrates the relationship between weighting coefficients and Knudsen number Kn .

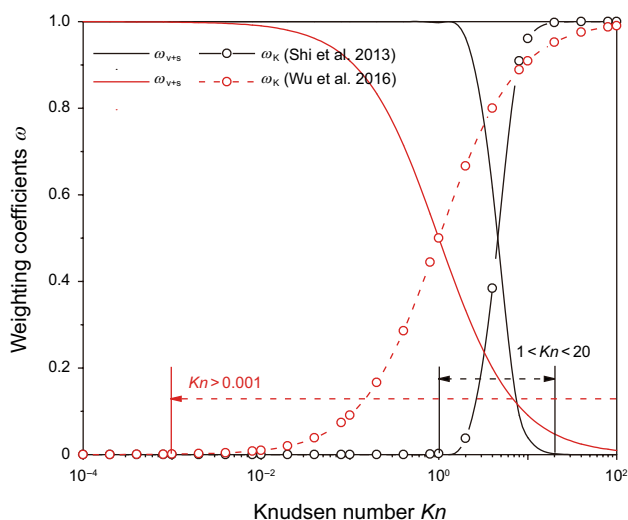


Fig. 3 Variation of weighting coefficients with different Knudsen number Kn

Figure 3 shows that Wu et al. (2016) model can describe Knudsen diffusion when Knudsen number ranges from 0.001 to 100, which is applicable to slip flow, transition flow, and free-molecular-flow regimes. Nevertheless, Shi et al. (2013) model can only describe Knudsen diffusion when Knudsen number ranges from 1 to 20, which neglects the probability of occurrence of Knudsen diffusion in the slip flow regime. Suitable weighting coefficients could describe gas transport behavior more accurately.

Thus, weighting coefficients presented in Wu et al. (2016) are applied, and Eq. (7) modified from Wu et al. (2016) can be rewritten as

$$J^I = -\frac{\phi_e^I}{\tau} \left[\frac{r_{eO}^2 p M}{8 \mu_e Z R T} \left(\frac{1 + \alpha Kn(IM)}{1 + Kn(IM)} \right) \left(1 + \frac{4Kn(IM)}{1 - bKn(IM)} \right) + \frac{2r_{eI} C_g}{3(1 + Kn(IM))} \left(\frac{8ZM}{\pi RT} \right)^{0.5} \frac{p}{Z} \right] \nabla p \tag{10}$$

2.2 Characterization of gas transport in OM

For adsorbed gas coexisting in pores, gas adsorption and surface diffusion are included as shown in Fig. 4.

The mass flux of free gas transport in OM can be expressed as

$$J_b^O = -\frac{\phi_e^O}{\tau} \left[\frac{r_{eO}^2 p M}{8 \mu_e Z R T} \left(\frac{1 + \alpha Kn(IM)}{1 + Kn(IM)} \right) \left(1 + \frac{4Kn(IM)}{1 - bKn(IM)} \right) + \frac{2r_{eI} C_g}{3(1 + Kn(IM))} \left(\frac{8ZM}{\pi RT} \right)^{0.5} \frac{p}{Z} \right] \nabla p. \tag{11}$$

where J_b^O is the bulk gas mass flux in OM, $kg/(m^2 s)$; and ϕ_e^O is the effective porosity of OM, dimensionless.

Both monolayer adsorption and multilayer adsorption have been found in shale reservoir conditions, and the adsorbed gas volume can be calculated by isotherm equation. Then, we can

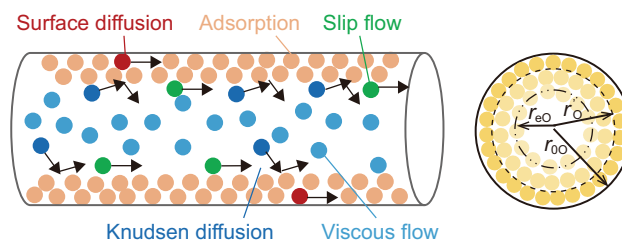


Fig. 4 Schematic diagram of gas transport in the OM nanopore

obtain the effective pore radius of the nanocapillary tube for free gas transport in OM.

Thus, the adsorption volume described by the BET isotherm equation is written as

$$V = V_L \frac{C \frac{p}{Z p_0} \left[1 - (n+1) \left(\frac{p}{Z p_0} \right)^n + n \left(\frac{p}{Z p_0} \right)^{n+1} \right]}{1 - \frac{p}{Z p_0} \left[1 + (C-1) \frac{p}{Z p_0} - C \left(\frac{p}{Z p_0} \right)^{n+1} \right]}, \tag{12}$$

where V is the adsorption volume of real gas in OM nanopores, m^3/kg ; V_L is the maximum adsorbed gas volume, m^3/kg ; C is a constant related to the net heat of adsorption, dimensionless; p_0 is the saturated adsorption pressure of the gas, MPa; and n is the adsorbed layer number, dimensionless. When $n = 1$, Eq. (12) is simplified as

$$V = V_L \frac{p/Z}{p_0/C + p/Z}. \tag{13}$$

If $p_0/C = p_L$, where p_L is the Langmuir pressure, MPa, Eq. (13) becomes the Langmuir isotherm. If $V/V_L = \theta$, the

effective pore radius as shown in Fig. 4 can be expressed as (detailed derivation presented in our previous work (Zhang et al. 2018)):

$$r_{eO} = \sqrt{r_{0O}^2 (1 - \theta) + \theta r_O'^2} \tag{14}$$

where r_{0O} is the original radius of organic nano-capillary tube, m; and for monolayer adsorption, the pore radius except first adsorption layer r_O' is defined as (Xiong et al. 2012)

$$r'_O = r_{O0} - \Gamma D_m, \tag{15}$$

where the gas coverage $\Gamma = \frac{p/Z}{p_L + p/Z}$.

The variation of the Knudsen number ratio $Kn(OM)/Kn(IM)$ with pore radius and pore pressure is shown in Fig. 5. The related parameters are set as $p_L = 4$ MPa, $C = 20$, $p_0 = 80$ MPa, $n = 2$.

As shown in Fig. 5, in the organic nanopore, when the pore pressure is less than 1 MPa, $Kn(OM)/Kn(IM) \approx 1$. It suggests that the decrease in the pore radius caused by adsorbed gas has a slight effect on gas transport behavior. When the pore pressure is greater than 1 MPa, $Kn(OM)/Kn(IM)$ increases with the increase in pore pressure and becomes larger than 1. Moreover, with the increase in pore radius, $Kn(OM)/Kn(IM)$ decreases at the same pore pressure. Xiong et al. (2012) model just considered monolayer adsorption by using the pore radius r'_O given by Eq. (16). Therefore, the results are greater than those calculated by the proposed model using the effective pore radius r_{eO} when $p < 20$ MPa. Meanwhile, $Kn(OM)/Kn(IM)$ of multilayer adsorption is smaller than that of monolayer adsorption when $p < 20$ MPa. When $p > 20$ MPa, $Kn(OM)/Kn(IM)$ of multilayer adsorption increases greatly and is much larger than that of monolayer adsorption. Additionally, as the pore radius increases, $Kn(OM)/Kn(IM)$ decreases, and especially, when the pore radius rises to 100 nm, $Kn(OM)/Kn(IM) \approx 1$, meaning the effects of adsorption on gas transport behaviors are negligible.

The surface diffusion flux for a real gas can be expressed as

$$J_s^O = -\frac{\phi_e^O}{\tau} \frac{r_{O0}^2}{r_{eO}^2} \frac{D_s M \rho_r V_L}{V_m} \frac{d\theta}{dp} \left(1 - \frac{r_{eO}^2}{r_{O0}^2} \right) \nabla p \tag{16}$$

where J_s^O is the mass flux of surface diffusion in OM nanopores, $kg/(m^2 s)$; D_s is the surface diffusion coefficient, m^2/s ; and ρ_r is the rock density, kg/m^3 .

The surface diffusion coefficient can be derived by the kinetic method under a high-pressure condition, and Chen and Yang (1991) presented the basic form as follows

$$D_s = D_s^0 \frac{(1 - \Gamma) + \frac{\kappa}{2} \Gamma (2 - \Gamma) + [H(1 - \kappa)](1 - \kappa) \frac{\kappa}{2} \Gamma^2}{\left(1 - \Gamma + \frac{\kappa}{2} \Gamma \right)^2}, \tag{17}$$

$$H(1 - \kappa) = \begin{cases} 0 & \kappa \geq 1 \\ 1 & 0 \leq \kappa \leq 1 \end{cases}, \tag{18}$$

$$\kappa = \frac{\kappa_b}{\kappa_m} \tag{19}$$

where D_s^0 is surface diffusion coefficient when $\Gamma = 0$, m^2/s . From Eqs. (18) and (19), it can be found that if $\kappa_b > \kappa_m$, $\kappa > 1$ and $H(1 - \kappa) = 0$ causing surface diffusion stop. When $\kappa_b < \kappa_m$, $\kappa < 1$, and $H(1 - \kappa) = 1$, surface diffusion occurs. Figure 6 shows the relationship among D_s/D_s^0 , Γ , and κ . With the increase in gas coverage Γ , D_s/D_s^0 increases at the same κ . When $\Gamma < 0.2$, κ influences D_s/D_s^0 slightly. However, when $\Gamma > 0.2$, smaller κ causes a larger D_s/D_s^0 at the same Γ , as shown in Fig. 6a. Besides, when $\Gamma > 0.4$, as κ increases, D_s/D_s^0 gradually decreases, as shown in Fig. 6b. Particularly, when $\Gamma = 1$, D_s/D_s^0 reduces sharply with the rising of κ . When $\Gamma < 0.4$, as κ increases, D_s/D_s^0 increases slightly.

Combining Eqs. (11) and (16), the total mass flux of a real gas transport in OM can be expressed as

$$J^O = J_b^O + J_s^O, \tag{20}$$

where J^O is the total mass flux of OM, $kg/(m^2 s)$.

In the parallel connection of organic and inorganic pores, the total gas mass flux can be expressed as

$$J_{I+O} = J^I + J^O \tag{21}$$

where J_{I+O} is the total mass flux of a nanoporous medium, $kg/(m^2 s)$.

We assume that the effective porosity of IM is ϕ_e^I , and the effective porosity of bulk gas in OM is ϕ_e^O .

The gas mass flux in a porous medium can be obtained by Darcy's law as

$$J_v = -\frac{pMk}{\mu ZRT} \nabla p, \quad k = \frac{r_0^2 \phi}{8\tau} \tag{22}$$

where k is the permeability, m^2 .

The AGP model in this work by comparing Eqs. (21) with (22) can be written as

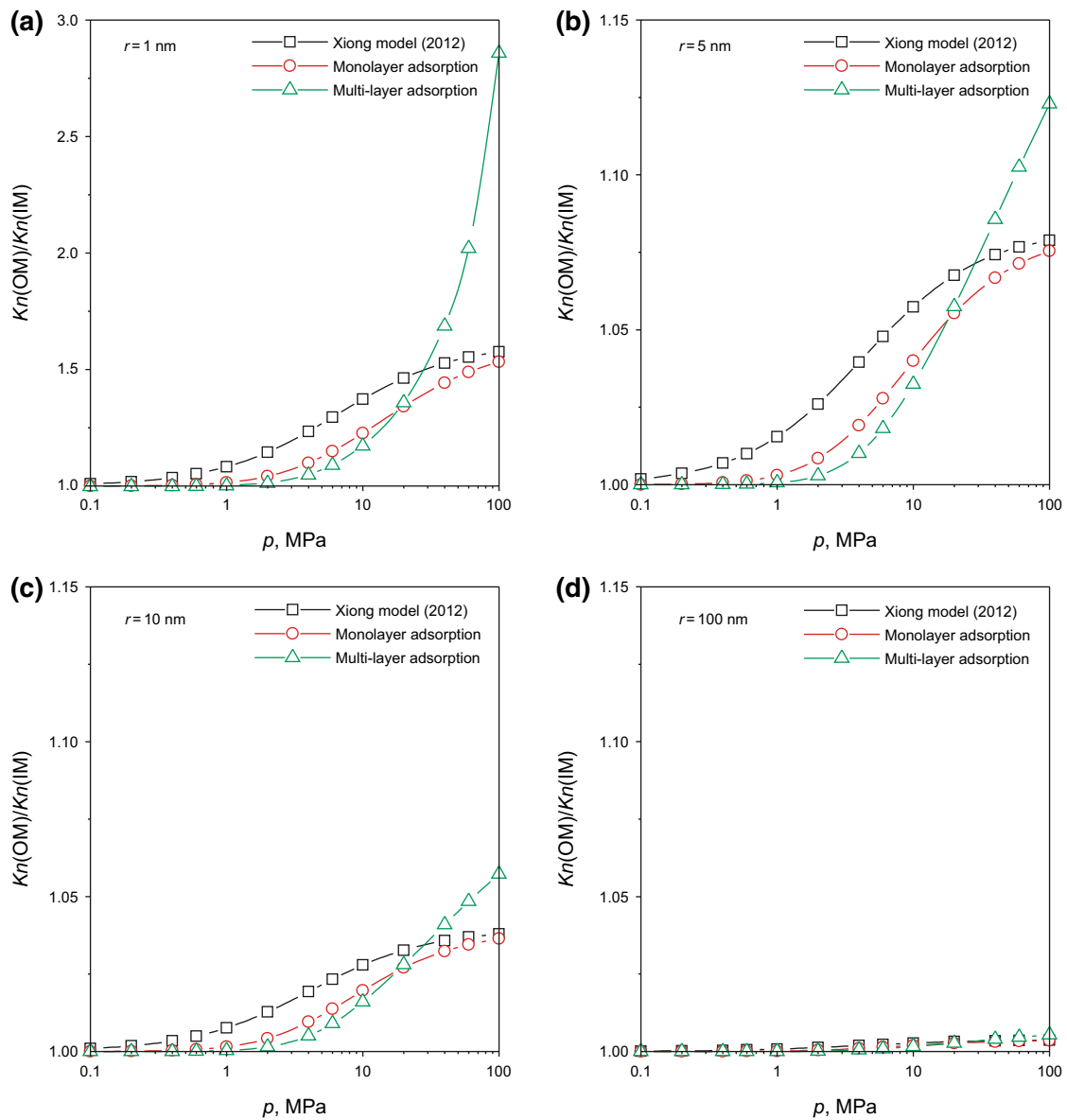


Fig. 5 Variation of the ratio $Kn(OM)/Kn(IM)$ with different pore radii and pressures

$$\begin{aligned}
 k_a = k_a^I + k_a^O = & \frac{\phi_c^I}{8\tau} \left[r_{cl}^2 \left(\frac{1 + \alpha Kn(IM)}{1 + Kn(IM)} \right) \left(1 + \frac{4Kn(IM)}{1 - bKn(IM)} \right) + \frac{16\mu r_{cl} C_g}{3(1 + 1/Kn(IM))} \left(\frac{8ZRT}{\pi M} \right)^{0.5} \right] \\
 & + \frac{\phi_c^O}{8\tau} \left[r_{eO}^2 \left(\frac{1 + \alpha Kn(OM)}{1 + Kn(OM)} \right) \left(1 + \frac{4Kn(OM)}{1 - bKn(OM)} \right) + \frac{16\mu r_{eO} C_g}{3(1 + 1/Kn(OM))} \left(\frac{8ZRT}{\pi M} \right)^{0.5} \right] \\
 & + \frac{\beta \phi \mu ZRT \rho_r V_L D_s}{\tau p V_m} \frac{d\theta}{dp} \left(1 - \frac{r_{eO}^2}{r_{OO}^2} \right),
 \end{aligned} \tag{23}$$

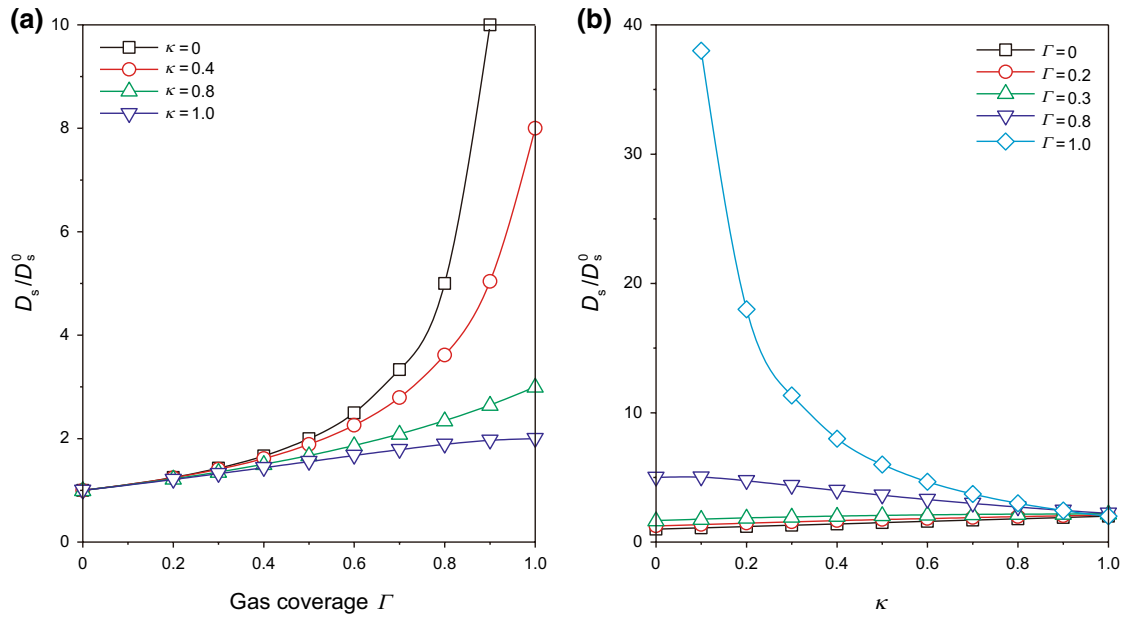


Fig. 6 The curves for D_s/D_s^0 versus Γ (a) and κ (b) of adsorbed gas

where k_a is the apparent permeability of nanopores, m^2 ; k_a^O is the apparent permeability of OM nanopores, m^2 ; and k_a^I is the apparent permeability of IM nanopores, m^2 .

The AGP of OM and IM is given by, respectively,

$$k_a^I = \frac{\phi_e^I}{8\tau} \left[r_{el}^2 \left(\frac{1 + \alpha Kn(IM)}{1 + Kn(IM)} \right) \left(1 + \frac{4Kn(IM)}{1 - bKn(IM)} \right) + \frac{16\mu r_{el} C_g}{3(1 + 1/Kn(IM))} \left(\frac{8ZRT}{\pi M} \right)^{0.5} \right], \quad (24)$$

$$k_a^O = \frac{\phi_e^O}{8\tau} \left[r_{eO}^2 \left(\frac{1 + \alpha Kn(OM)}{1 + Kn(OM)} \right) \left(1 + \frac{4Kn(OM)}{1 - bKn(OM)} \right) + \frac{16\mu r_{eO} C_g}{3(1 + 1/Kn(OM))} \left(\frac{8ZRT}{\pi M} \right)^{0.5} \right] + \frac{\beta \phi \mu ZRT \rho_r V_L D_s}{\tau p V_m} \frac{d\theta}{dp} \left(1 - \frac{r_{eO}^2}{r_{00}^2} \right). \quad (25)$$

The pore radius considering the stress dependence can be given by (detailed derivation in “Appendix”):

$$r = r_0 (p_e/p')^{\frac{q-s}{2}}, \quad (26)$$

where r_0 is the original radius of the nanopore, m; p_e is the effective stress, MPa; p' is the atmospheric pressure MPa; q is the porosity coefficient, dimensionless; and s is the permeability coefficient, dimensionless.

3 Analysis of gas transport behavior in shale

3.1 Model verification

The experimental results (Tison 1993) and results obtained from the linearized Boltzmann (Loyalka and

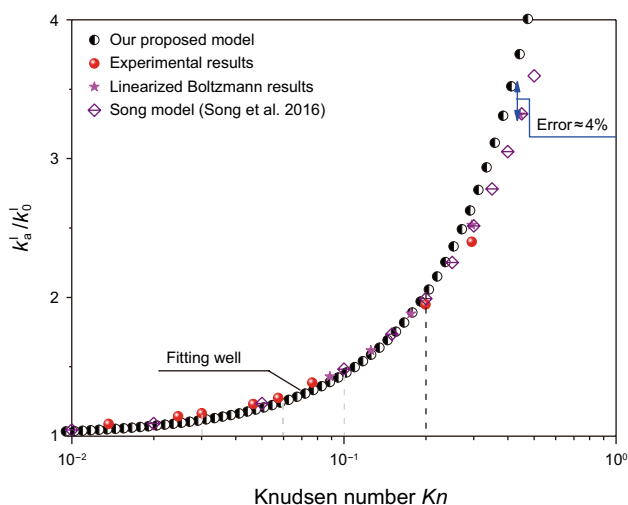


Fig. 7 Validation of the presented AGP model

Table 2 Various parameters used in this section

Parameter	Value	Parameter	Value
Tortuosity τ	2.0	Permeability coefficient s	0
Constant related to net heat of adsorption C	20	Surface diffusion coefficient $D_s, \text{m}^2/\text{s}$	1×10^{-6}
Temperature T, K	353	Langmuir volume $V_L, \text{m}^3/\text{kg}$	2.83×10^{-3}
Deviation factor Z	1.0	Gas viscosity $\mu, \text{mPa s}$	1
Saturated adsorption pressure of gas p_0, MPa	80	Rock density $\rho_r, \text{kg}/\text{m}^3$	$2.6 \times 10^3 \text{ kg}/\text{m}^3$
OM porosity ϕ_e^O	0.01	Gas slip constant b	-1
IM porosity ϕ_e^I	0.04	Langmuir pressure p_L, MPa	4
Total porosity	0.05	Gas molecule diameter D_m, nm	0.38
Underburned pressure p_o, MPa	45	Adsorption layer n	1
Pore radius of the nanoporous medium r_0, nm	1	Methane molar mass $M, \text{kg}/\text{mol}$	0.016
Porosity coefficient q	0	Methane molar volume $V_m, \text{m}^3/\text{mol}$	0.02237

Hamoodi 1990) and Song et al. model (Song et al. 2016) were used to validate the presented model in this study. The validation indicates that the proposed AGP model in this work is reliable in describing gas transport behavior in nanopores, especially when the Knudsen number is less than 0.2 (Fig. 7).

3.2 Sensitivity analysis

3.2.1 Influences of pore radius and pressure on gas transport behavior

The influences of various parameters can be analyzed based on the parameters given in Table 2.

The permeability ratio k_a^I/k_0^I decreases as the pore radius increases when the pore pressure is 0.1–30 MPa, as shown in Fig. 8a. When $r > 5 \mu\text{m}$, $k_a^I/k_0^I \approx 1$ at any pore pressure

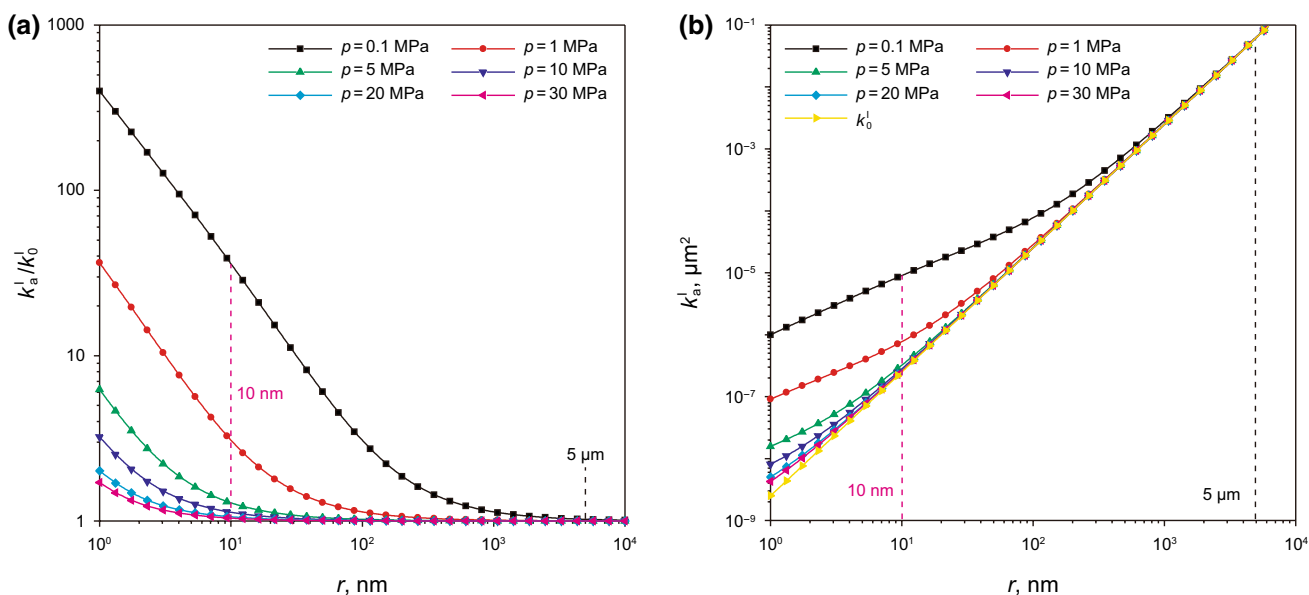


Fig. 8 The AGP of IM nanopores versus pore radius

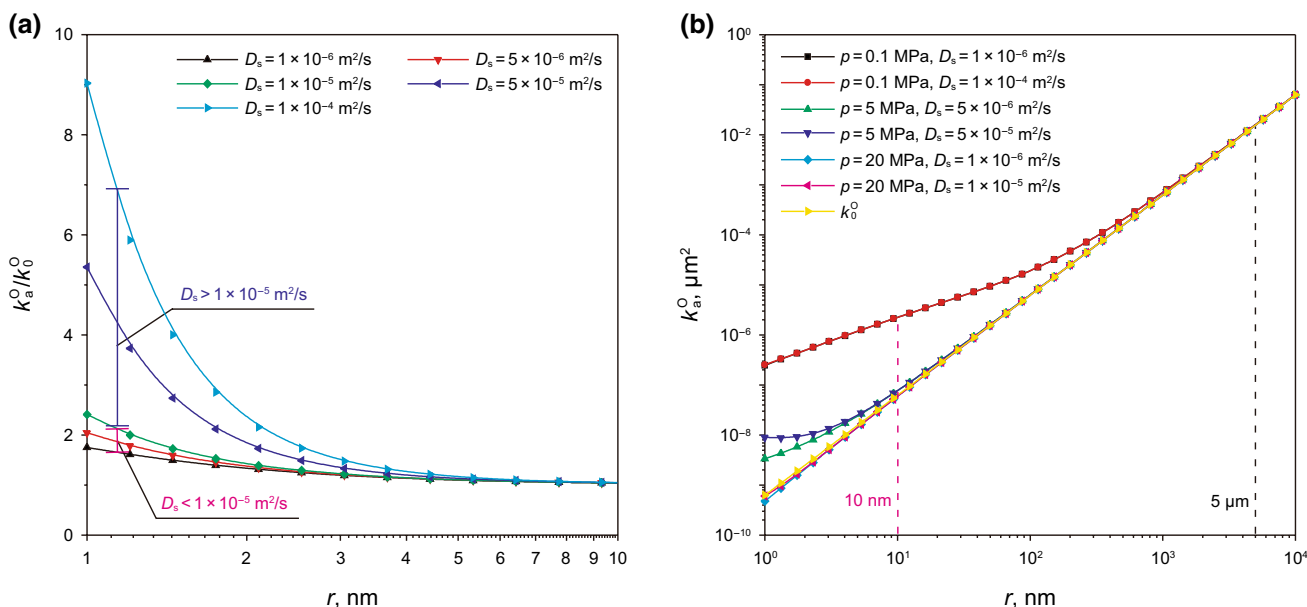


Fig. 9 The AGP of OM nanopores versus pore radius under different pore pressures and surface diffusion coefficients

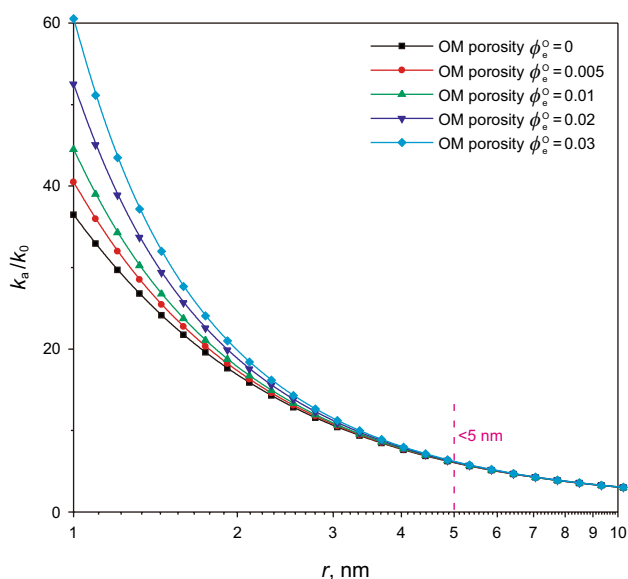


Fig. 10 Variation of k_a/k_0 with pore radius under different OM porosities

greater than 0.1 MPa. Then, the larger the pore pressure is, the smaller the pore radius is when $k_a^I/k_0^I \approx 1$. When $r < 10$ nm, k_a^I/k_0^I is larger than 1 at any pore pressure less than 30 MPa. Meanwhile, as shown in Fig. 8b, the AGP of IM increases with an increase in pore radius and then is equal to the intrinsic permeability at a certain pore radius. Moreover, a smaller pore pressure leads to a larger AGP at the same pore radius condition.

As shown in Fig. 9a, the surface diffusion coefficient D_s affects the gas transport behavior when $r < 10$ nm and pore pressure is equal to 10 MPa. The larger surface diffusion coefficient D_s , the greater k_a^O/k_0^O is under the same pore radius condition. However, when the surface diffusion coefficient D_s is less than 1×10^{-5} m²/s, it has a little effect on the AGP. Figure 9b shows that when $p = 0.1$ MPa or $r < 10$ nm, the effect of D_s can be ignored. In addition, under the same pore pressure condition, the AGP of OM nanopores increases with an increase in D_s .

3.2.2 Influences of OM porosity, temperature, and stress dependence on gas transport behavior

The OM porosity influences gas transport behavior in nanoporous shale through the gas adsorption and surface diffusion.

If the surface diffusion coefficient D_s is set as 1×10^{-4} m²/s, and the pore pressure is 1 MPa, the ratio of total AGP to intrinsic permeability of the nanoporous shale k_a/k_0 decreases slightly with the OM porosity increase when $r < 5$ nm. This suggests that the gas adsorption and small surface diffusion coefficient cause the AGP of OM smaller than that of IM, as shown in Fig. 10. The effects of the OM porosity and surface diffusion coefficient on gas transport behavior are analyzed in the next section.

As shown in Fig. 11a, there are slight differences k_a/k_0 under four different temperature conditions when $r < 10$ nm and $p = 1$ MPa. With an increase in temperature, k_a/k_0 increases. Furthermore, with an increase in pressure, the weighting coefficient of the Knudsen diffusion decreases,

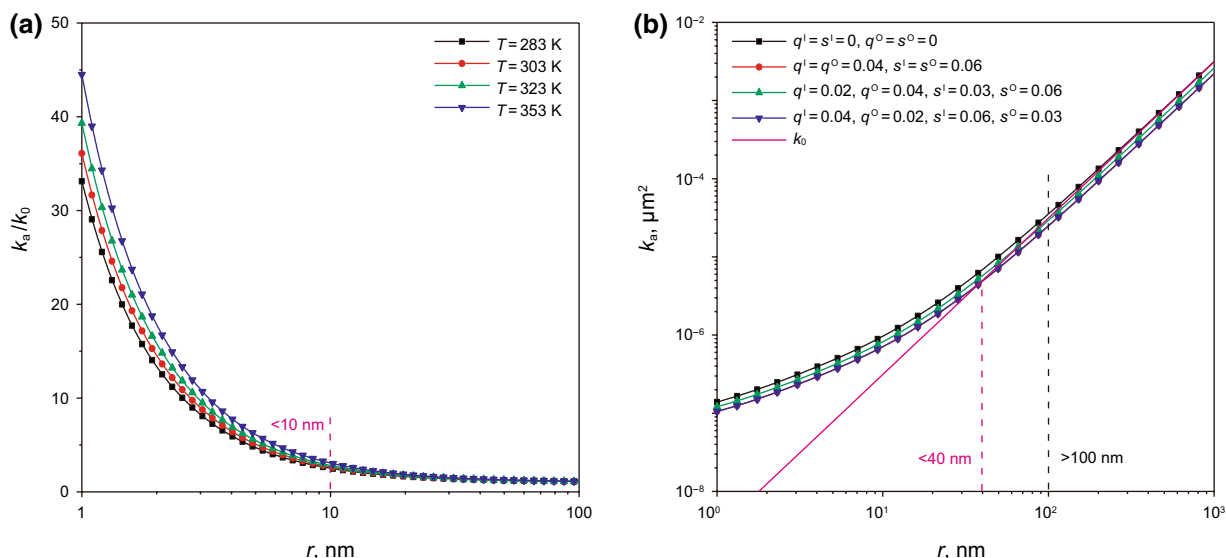


Fig. 11 Variation of k_a/k_0 with pore radius under different temperature conditions (a), porosity and permeability coefficients (b)

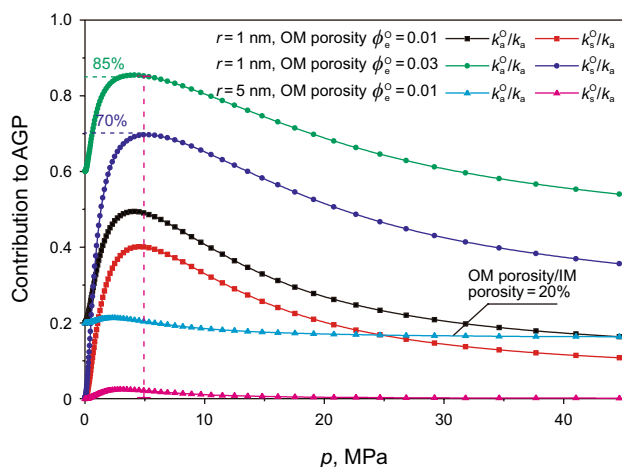


Fig. 12 Variation of the contributions of surface diffusion and OM to the total AGP with pore pressure under different r and D_s

which leads to a decrease in k_a/k_0 . This suggests that the influence of temperature on gas transport behavior should be considered under small pore radius conditions.

With the development of shale gas reservoirs, the stress dependence will occur in nanopores. Hence, different porosity and permeability coefficients of OM and IM nanopores are set to discuss the influence of stress dependence on the total AGP, as shown in Fig. 11b. When $r < 40$ nm, the total AGP is larger than the intrinsic permeability. This is because the total AGP is mainly affected by the Knudsen diffusion and surface diffusion. Moreover, considering the stress dependence, the total AGP is smaller than that without consideration of stress

dependence. Additionally, when the porosity and permeability coefficients of IM nanopores $q^I > q^O$ and $s^I > s^O$, the total AGP is smaller than that if $q^I < q^O$ and $s^I < s^O$. This is because the stress dependence not only affects the gas viscous flow and slip flow in nanopores but also the Knudsen diffusion and surface diffusion. To a certain extent, the total AGP is affected by the surface diffusion coefficient and OM porosity.

3.3 Contributions of different mechanisms to the total AGP

Based on the above derivation, the ratio of each mechanism to the total AGP can be obtained. k_s^O is the apparent permeability of surface diffusion in OM, m^2 ; k_K^{I+O} is the apparent permeability of Knudsen diffusion in nanopores, m^2 ; and k_{v+s}^{I+O} is the apparent permeability of viscous and slip flow in nanopores, m^2 . The surface diffusion coefficient has a significant influence on the contribution of OM AGP to the total AGP. The influence of the OM porosity on gas transport behavior is discussed in Fig. 12. When $D_s = 1 \times 10^{-4} m^2/s$, k_a^O/k_a increases as the OM porosity increases, and the surface diffusion dominates the OM AGP. If $r = 1$ nm, OM porosity $\phi_e^O = 0.03$ and IM porosity $\phi_e^I = 0.02$, $k_a^O/k_a \approx 85\%$ when $p = 5$ MPa, and k_s^O/k_a is about 70%. Therefore, when the pore radius is small, the gas transport in OM nanopores dominates the total AGP under the large surface diffusion coefficient and high OM porosity.

Figure 13 shows the contributions for three mechanisms and two pore types versus pore pressure under different pore radii (2 and 5 nm) and different pore pressures (1 and 20 MPa) when $D_s = 1 \times 10^{-4} m^2/s$, OM porosity $\phi_e^O = 0.01$, and IM

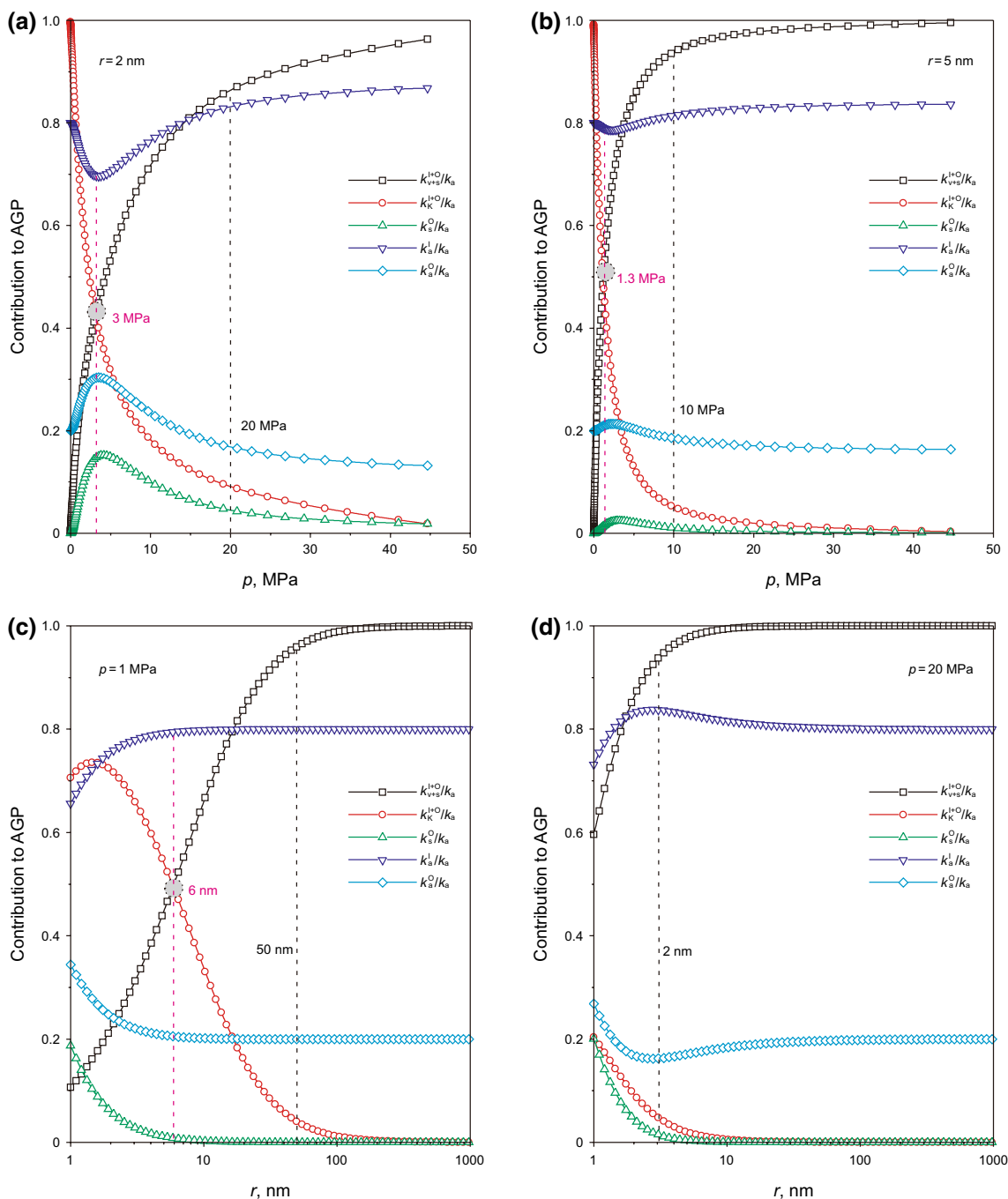


Fig. 13 Comparison of different permeability ratios with pore pressure and pore radius under different conditions ($D_s = 1 \times 10^{-4}$ m²/s, OM porosity=0.01, IM porosity=0.04)

porosity $\phi_c^I = 0.04$. In Fig. 13a, for pore radius of 2 nm, the increasing pore pressure decreases the Knudsen diffusion ratio k_K^{I+O}/k_a and increases the viscous–slip flow ratio k_{v+s}^{I+O}/k_a . The viscous–slip flow dominates gas transport when $p > 20$ MPa. For the pore radius of 5 nm, the viscous–slip flow is dominant at a smaller pore pressure (10 MPa) than that in the pore with 2 nm radius in Fig. 13b.

When the pore pressure is 1 MPa, the Knudsen diffusion still dominates in the pores with a radius smaller than 10 nm. k_K^{I+O}/k_a increases first and decreases later with an increase in pore radius, as shown in Fig. 13c. When the pore pressure continues to increase, as shown in Fig. 13d, the peak of k_K^{I+O}/k_a drops, and the surface diffusion, Knudsen diffusion, and viscous–slip diffusion collectively govern gas transport behavior in pores with a radius smaller than 10 nm. Moreover,

the pore radius range in which the viscous–slip flow dominates is larger with an increase in pore pressure. The influences of surface diffusion and Knudsen diffusion on gas transport can be neglected in the pores with a radius smaller than 10 nm.

4 Conclusions

In this study, a unified gas transport model in the parallel connection of inorganic and organic shale nanopores was developed. The model was validated by the experimental results. According to the discussion of the results, the following conclusions can be drawn:

1. The parallel connection of inorganic and organic nanopores is introduced into the AGP model to characterize the coexistence of different pore types in shale gas reservoirs. Otherwise, weighting coefficients based on Knudsen number are considered. The effect of adsorbed gas on $Kn(OM)/Kn(IM)$ can be neglected when $p < 1$ MPa or $r > 100$ nm. When 1 MPa $< p < 20$ MPa, $Kn(OM)/Kn(IM)$ caused by multilayer adsorption is lowest and then becomes largest if $p > 40$ MPa.
2. By validating the proposed model with experimental results, the weighting coefficients and surface diffusion equation can be accepted. The proposed model can be used to analyze different gas transport mechanisms in nanoporous shale and microsimulation in the shale gas reservoirs.
3. The pore radius and pressure have significant influences on the AGP. The larger pore radius or the larger pressure causes the smaller k_a/k_0 , meaning the viscous flow dominates gas transport. The surface diffusion has a large effect on gas transport behavior in nanopores with a radius less than 10 nm when $D_s > 1 \times 10^{-5}$ m²/s. The OM porosity affects k_a/k_0 slightly when the pore radius is larger than 5 nm. Additionally, the temperature has a small effect on gas transport behavior.
4. When the pore radius is the same, the larger the OM porosity is, the greater the value of k_s^O/k_a is. For a small pore and a low pressure, the surface diffusion and Knudsen diffusion are dominant. When the pore is larger and pressure is higher, gas transport behavior is controlled by viscous flow.

Considering the complex fracture network around the horizontal well in shale reservoirs (Zeng et al. 2016, 2018), the presented model can be coupled with the natural fracture system and hydraulic fracture network to simulate the field scale development.

Acknowledgements The authors would like to acknowledge financial support from the Fundamental Research Funds for the

Central Universities (China University of Geosciences, Wuhan) (No. CUGGC04), National Natural Science Foundation of China (No. 51904279), and Foundation of Key Laboratory of Tectonics and Petroleum Resources (China University of Geosciences) (No. TPR-2019-03).

Open Access This article is distributed under the terms of the Creative Commons Attribution 4.0 International License (<http://creativecommons.org/licenses/by/4.0/>), which permits unrestricted use, distribution, and reproduction in any medium, provided you give appropriate credit to the original author(s) and the source, provide a link to the Creative Commons license, and indicate if changes were made.

Appendix: Derivation of the pore radius considering the stress dependence

With the development of shale gas reservoirs, the effective stress increases, causing the decrease in the intrinsic permeability, porosity, and pore radius. Wu et al. (2016) applied the power–law relationships of shale core stress sensitive tests conducted by Dong et al. (2010) to consider the stress dependence, which can be expressed as

$$k = k_0(p_e/p')^{-s} \tag{A.1}$$

$$\phi = \phi_0(p_e/p')^{-q} \tag{A.2}$$

$$p_e = p_0 - p \tag{A.3}$$

where k is the permeability, m²; k_0 is the intrinsic permeability of a nanoporous medium, m²; and p_0 is the overburden pressure, MPa.

The relationship among the pore radius, permeability, and porosity is given by

$$k = \frac{\phi r^2}{8\tau} \tag{A.4}$$

Combining Eqs. (A.1), (A.2) with (A.3), the effective pore radius of IM and OM can be written as, respectively,

$$r_{eI} = r_{oI} = r_0(p_e/p')^{\frac{q-s}{2}} \tag{A.5}$$

$$r_{oO} = r_0(p_e/p')^{\frac{q-s}{2}} \tag{A.6}$$

where r_{oI} is the radius of an inorganic nanopore, m.

References

- Akkutulu IY, Fathi E. Multiscale gas transport in shales with local kerogen heterogeneities. SPE J. 2012;17(4):1002–11. <https://doi.org/10.2118/146422-PA>.
- Ambrose RJ, Hartman RC, Diaz-Campos M, Akkutlu I, Sondergeld C. Shale gas-in-place calculations part I: new

- pore-scale considerations. *SPE J.* 2012;17(1):219–29. <https://doi.org/10.2118/131772-PA>.
- Beskok A, Karniadakis GE. Report: a model for flows in channels, pipes, and ducts at micro and nano scales. *Microscale Thermophys Eng.* 1999;3:43–77. <https://doi.org/10.1080/108939599199864>.
- Bird GA. *Molecular gas dynamics and the direct simulation of gas flows*. Oxford: Oxford University Press; 1994.
- Botan A, Vermorel R, Ulm FJ, Pellenq RJM. Molecular simulations of supercritical fluid permeation through disordered microporous carbons. *Langmuir.* 2013;29(32):9985–90. <https://doi.org/10.1021/la402087r>.
- Chen L, Zhang L, Kang Q, Viswanathan HS, Yao J, Tao W. Nanoscale simulation of shale transport properties using the lattice Boltzmann method: permeability and diffusivity. *Sci Rep.* 2015;5:8089. <https://doi.org/10.1038/srep08089>.
- Chen YD, Yang RT. Concentration dependence of surface diffusion and zeolitic diffusion. *AIChE J.* 1991;37(10):1579–82. <https://doi.org/10.1002/aic.690371015>.
- Civan F. Effective correlation of apparent gas permeability in tight porous media. *Transp Porous Media.* 2010;82:375–84. <https://doi.org/10.1007/s11242-009-9432-z>.
- Civan F, Rai CS, Sondergeld CH. Shale-gas permeability and diffusivity inferred by improved formulation of relevant retention and transport mechanisms. *Transp Porous Media.* 2011;86:925–44. <https://doi.org/10.1007/s11242-010-9665-x>.
- Civan F, Devegowda D, Sigal RF. Critical evaluation and improvement of methods for determination of matrix permeability of shale. In: *SPE annual technical conference and exhibition*, 30 September–2 October, New Orleans, Louisiana; 2013. <https://doi.org/10.2118/166473-MS>.
- Darabi H, Eftehad A, Javadpour F, Sepehrnoori K. Gas flow in ultratight shale strata. *J Fluid Mech.* 2012;710:641–58. <https://doi.org/10.1017/jfm.2012.424>.
- Dong J, Hsu J, Wu W, Shimamoto T, Hung J, Yeh E, et al. Stress dependence of the permeability and porosity of sandstone and shale from TCDP Hole-A. *Int J Rock Mech Min Sci.* 2010;47(7):1141–57. <https://doi.org/10.1016/j.ijrmm.2010.06.019>.
- Javadpour F. Nanopores and apparent permeability of gas flow in mudrocks (shales and siltstone). *J Can Pet Technol.* 2009;48(8):16–21. <https://doi.org/10.2118/09-08-16-DA>.
- Karniadakis G, Beskok A, Aluru N. *Microflows and nanoflows: fundamentals and simulation*. Berlin: Springer; 2005.
- Lee AL, Gonzalez MH, Eakin BE. The viscosity of natural gases. *J Petrol Technol.* 1966;18(8):997–1000. <https://doi.org/10.2118/1340-PA>.
- Li J, Ding D, Wu YS, Di Yuan. A generalized framework model for the simulation of gas production in unconventional gas reservoirs. In: *SPE reservoir simulation symposium*, 18–20 February, The Woodlands, Texas; 2013. <https://doi.org/10.2118/163609-PA>.
- Loyalka SK, Hamoodi SA. Poiseuille flow of a rarefied gas in a cylindrical tube: solution of linearized Boltzmann equation. *Phys Fluids A.* 1990;2:2061–5. <https://doi.org/10.1063/1.857681>.
- Mahmoud M. Development of a new correlation of gas compressibility factor (Z factor) for high pressure gas reservoirs. *J Energy Res Technol.* 2014;136:012903. <https://doi.org/10.1115/1.4025019>.
- Michel GG, Sigal RF, Civan F, Devegowda D. Parametric investigation of shale gas production considering nano-scale pore size distribution, formation factor, and non-Darcy flow mechanisms. In: *SPE annual technical conference and exhibition*, 30 October–2 November, Denver, Colorado, USA; 2011. <https://doi.org/10.2118/147438-MS>.
- Shi J, Zhang L, Li Y, Yu W, He X, Liu N, et al. Diffusion and flow mechanisms of shale gas through matrix pores and gas production forecasting. In: *SPE unconventional resources conference* Canada, 5–7 November, Calgary, Alberta; 2013. <https://doi.org/10.2118/167226-MS>.
- Sigal RF. The effects of gas adsorption on storage and transport of methane in organic shales. In: *SPWLA 54th annual logging symposium*, 22–26 June, New Orleans; 2013.
- Singh H, Javadpour F. Langmuir slip-Langmuir sorption permeability model of shale. *Fuel.* 2016;164:28–37. <https://doi.org/10.1016/j.fuel.2015.09.073>.
- Song W, Yao J, Li Y, Sun H, Zhang L, Yang Y, et al. Apparent gas permeability in an organic-rich shale reservoir. *Fuel.* 2016;181:973–84. <https://doi.org/10.1016/j.fuel.2016.05.011>.
- Su Y, Zhang Q, Wang W, Sheng G. Performance analysis of a composite dual-porosity model in multi-scale fractured shale reservoir. *J Nat Gas Sci Eng.* 2015;26:1107–18. <https://doi.org/10.1016/j.jngse.2015.07.046>.
- Sun H, Yao J, Cao Y, Fan DY, Zhang L. Characterization of gas transport behaviors in shale gas and tight gas reservoirs by digital rock analysis. *Int J Heat Mass Transf.* 2017;104:227–39. <https://doi.org/10.1016/j.ijheatmasstransfer.2016.07.083>.
- Tison SA. Experimental data and theoretical modeling of gas flows through metal capillary leaks. *Vacuum.* 1993;44:1171–5.
- Wang J, Liu H, Wang L, Zhang H, Luo H, Gao Y. Apparent permeability for gas transport in nanopores of organic shale reservoirs including multiple effects. *Int J Coal Geol.* 2015;152(3):50–62. <https://doi.org/10.1016/j.coal.2015.10.004>.
- Wang J, Yang Z, Dong M, Gong H, Sang Q, Li Y. Experimental and numerical investigation of dynamic gas adsorption/desorption–diffusion process in shale. *Energy Fuels.* 2016a;30(12):10080–91. <https://doi.org/10.1021/acs.energyfuels.6b01447>.
- Wang J, Dong M, Yang Z, Gong H, Li Y. Investigation of methane desorption and its effect on the gas production process from shale: experimental and mathematical study. *Energy Fuel.* 2016b;31(1):205–16.
- Wang J, Yuan Q, Dong M, Cai J, Yu L. Experimental investigation of gas mass transport and diffusion coefficients in porous media with nanopores. *Int J Heat Mass Transf.* 2017;115:566–79. <https://doi.org/10.1016/j.ijheatmasstransfer.2017.08.05>.
- Wu K, Li X, Wang C, Yu W, Guo C, Ji D, et al. Apparent permeability for gas flow in shale reservoirs coupling effects of gas diffusion and desorption. In: *SPE/AAPG/SEG unconventional resources technology conference*, 25–27 August, Denver, Colorado; 2014. <https://doi.org/10.15530/URTEC-2014-1921039>.
- Wu K, Chen Z, Li X. Real gas transport through nanopores of varying cross-section type and shape in shale gas reservoirs. *Chem Eng J.* 2015a;281:813–25. <https://doi.org/10.1016/j.cej.2015.07.012>.
- Wu K, Li X, Wang C, Chen Z, Yu W. A model for gas transport in microfractures of shale and tight gas reservoirs. *Transp Phenom Fluid Mech.* 2015b;61(6):2079–88. <https://doi.org/10.1002/aic.14791>.
- Wu K, Chen Z, Wang H, Yang S, Li X, Shi J. A model for real gas transfer in nanopores of shale gas reservoirs. In: *EUROPEC 2015*, 1–4 June, Madrid; 2015c. <https://doi.org/10.2118/174293-MS>.
- Wu K, Chen Z, Li X, Guo C, Wei M. A model for multiple transport mechanisms through nanopores of shale gas reservoirs with real gas effect–adsorption-mechanic coupling. *Int J Heat Mass Transf.* 2016;93:408–26.
- Wu K, Chen Z, Li X, Xu J, Li J, Wang K, et al. Flow behavior of gas confined in nanoporous shale at high pressure: real gas effect. *Fuel.* 2017;205:173–83.
- Xiong X, Devegowda D, Michel GG, Sigal RF, Civan F. A fully-coupled free and adsorptive phase transport model for shale gas reservoirs including non-Darcy flow effects. In: *SPE annual technical conference and exhibition*, 8–10 October, San Antonio, Texas; 2012. <https://doi.org/10.2118/159758-MS>.
- Yao J, Sun H, Fan D, Wang C, Sun Z. Numerical simulation of gas transport mechanisms in tight shale gas reservoir. *Pet*

- Sci. 2013;10(4):528–37. <https://doi.org/10.1007/s12182-013-0304-3>.
- Zeng F, Cheng X, Guo J, Long C, Ke YB. A new model to predict the unsteady production of fractured horizontal wells. *Sains Malaysiana*. 2016;45(10):1579–87.
- Zeng F, Guo J, Ma S, Chen Z. 3D observations of the hydraulic fracturing process for a model non-cemented horizontal well under true triaxial conditions using an X-ray CT imaging technique. *J Nat Gas Sci Eng*. 2018;52:128–40. <https://doi.org/10.1016/j.jngse.2018.01.033>.
- Zhang Q, Su Y, Wang W, Lu M, Sheng G. Apparent permeability for liquid transport in nanopores of shale reservoirs: coupling flow enhancement and near wall flow. *Int J Heat Mass Transf*. 2017;115B:224–34. <https://doi.org/10.1016/j.ijheatmasstransfer.2017.08.024>.
- Zhang Q, Su Y, Wang W, Lu M, Sheng G. Gas transport behaviors in shale nanopores based on multiple mechanisms and macroscale modeling. *Int J Heat Mass Transf*. 2018;125:845–57. <https://doi.org/10.1016/j.ijheatmasstransfer.2018.04.129>.
- Zou C, Zhu R, Wu S, Yang Z, Tao S, Yuan X. Type, characteristics, genesis and prospects of conventional and unconventional hydrocarbon accumulations: taking tight oil and tight gas in China as an instance. *Acta Pet Sin*. 2012;33:173–87. <https://doi.org/10.7623/syxb201202001> (in Chinese).